JACS
JOURNAL OF THE AMERICAN CHEMICAL SOCIETY
Article
pubs.acs.org/JACS

High *ZT* in p-Type $(PbTe)_{1-2x}(PbSe)_x(PbS)_x$ Thermoelectric Materials

Rachel J. Korkosz,[†] Thomas C. Chasapis,[†] Shih-han Lo,[‡] Jeff W. Doak,[‡] Yoon Jun Kim,[‡] Chun-I Wu,[∥] Euripidis Hatzikraniotis,[§] Timothy P. Hogan,[∥] David N. Seidman,[‡] Chris Wolverton,[‡] Vinayak P. Dravid,[‡] and Mercouri G. Kanatzidis*[,†]

[†]Department of Chemistry, and [‡]Department of Materials Science and Engineering, Northwestern University, Evanston, Illinois 60208, United States

[§]Department of Physics, Aristotle University of Thessaloniki, 54124 Thessaloniki, Greece

[∥]Department of Electrical and Computer Engineering, Michigan State University, East Lansing, Michigan 48824, United States

Supporting Information

ABSTRACT: Lead chalcogenide thermoelectric systems have been shown to reach record high figure of merit values via modification of the band structure to increase the power factor or via nanostructuring to reduce the thermal conductivity. Recently, $(PbTe)_{1-x}(PbSe)_x$ was reported to reach high power factors via a delayed onset of interband crossing. Conversely, the $(PbTe)_{1-x}(PbS)_x$ was reported to achieve low thermal conductivities arising from extensive nanostructuring. Here we report the thermoelectric properties of the pseudoternary 2% Na-doped $(PbTe)_{1-2x}(PbSe)_x(PbS)_x$ system. The $(PbTe)_{1-2x}(PbSe)_x(PbS)_x$ system is an excellent platform to study phase competition between entropically driven atomic mixing (solid solution behavior) and enthalpy-driven phase separation. We observe that the thermoelectric properties of the PbTe−PbSe−PbS 2% Na doped are superior to those of 2% Na-doped PbTe−PbSe and PbTe−PbS, respectively, achieving a *ZT* ≈2.0 at 800 K. The material exhibits an increased the power factor by virtue of valence band modification combined with a very reduced lattice thermal conductivity deriving from alloy scattering and point defects. The presence of sulfide ions in the rock-salt structure alters the band structure and creates a plateau in the electrical conductivity and thermopower from 600 to 800 K giving a power factor of 27 μW/cmK^2. The very low total thermal conductivity values of 1.1 W/m·K of the x = 0.07 composition is accounted for essentially by phonon scattering from solid solution defects rather than the assistance of endotaxial nanostructures.

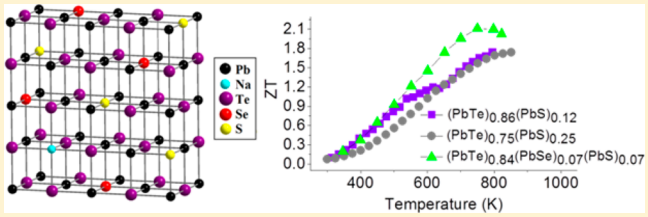

INTRODUCTION

Thermoelectric materials provide a means of direct electrical power generation from sources of heat, making them particularly appealing in waste heat recovery. The efficiency of a thermoelectric material is related to the figure of merit, $ZT = (S^2\sigma T/\kappa)$, where T is the operating temperature, S is the Seebeck coefficient or thermopower, σ is the electrical conductivity, and κ is the thermal conductivity. Effective strategies for improving *ZT* involve decreasing the thermal conductivity by introducing substitutional alloying on specific crystallographic sites in the structure and at the same time inducing nanostructures in the matrix as scattering centers to reduce the mean free path of heat carrying phonons. Nanostructuring in a bulk material was first reported in the system $AgPb_mSbTe_{2+m}$ (LAST), even though PbTe−$AgSbTe_2$ was previously believed to be a solid solution.[1−4] The nanostructures in this system increased the *ZT* to 1.7 for $AgPb_{18}SbTe_{20}$ at 723 K and *ZT* ≈ 1.6 at 650 K in the sister system $Na_{0.95}Pb_{20}SbTe_{22}$ (SALT) compared to *ZT* ≈ 1 for n-type PbTe and ≈1.5−1.7 p-type PbTe.[1,5−9] Additionally, Na doping is known to introduce point defects and nanoscale precipitates in the binary lead chalcogenides PbTe, PbSe, and PbS as well as PbTe−PbS and other PbQ- based alloys.[10−12] Subsequently, nanostructures have been incorporated in many systems or observed in systems which previously were thought to be solid solutions. Examples include Na-doped PbTe−PbS,[12−14] PbTe−(Ca,Ba,Sr)Te,[15,16] PbSe−Cd(Se,S),[17] PbSe−Zn(Se,S),[17] PbSe−(Ca,Sr,Ba)Te,[17] PbS−(Cd,Zn)S,[18] PbS−(Ca,Sr)S,[11] and Na-free PbSe−PbS[19] and PbS−PbTe.[20] The nanostructures induced by simple Na doping in binary PbQ phases are not effective phonon scatterers and do not substantially reduce the lattice thermal conductivity.[10,21]

The thermopower and electrical conductivity of degenerately doped semiconductor thermoelectric materials are interrelated through the carrier concentration and the density of states (DOS) effective mass. The carrier concentration must be selected to balance the inverse relationship between electrical conductivity and thermopower to maximize the power factor ($S^2\sigma$). Decoupling these relationships by increasing the thermopower without adversely affecting the electronic conductivity is possible primarily through altering the band structure either via increased band degeneracy[22] or other modification of the light- and heavy-hole valence band.[23,24] In heavily doped p-type PbTe, interplay between the light- and heavy-hole valence bands can result in significant increases in

Received: December 3, 2013
Published: February 17, 2014

 © 2014 American Chemical Society dx.doi.org/10.1021/ja4121583 | *J. Am. Chem. Soc.* 2014, 136, 3225−3237

the power factor at high temperature.[25] These methods of band structure engineering can increase the power factor and ZT significantly. For example, Tl-doped PbTe reaches $ZT \approx 1.5$ at 773 K.[26] Tl in $PbTe_{(1-x)}PbSe_{(x)}$ and $PbTe_{(1-x)}PbS_{(x)}$ have also been shown to produce enhanced $ZT = 1.6$ at 700 K.[27] Alloying PbTe and PbSe alters the convergence temperature of the light and heavy hole valence bands in PbTe. By increasing the convergence temperature compared to PbTe the power factor is maximized at a higher temperature resulting in $ZT \approx 1.8$ at 850 K.[22]

In the family of lead chalcogenides, the pseudobinary systems PbTe−PbS,[12−14,28] PbTe−PbSe,[22,29] and PbSe−PbS[19] have been studied and developed to a state of remarkably high performance. PbTe−PbS exhibits well-defined nanostructuring both on the PbTe-rich side of the composition where PbTe is the matrix and PbS is the second phase and on the PbS-rich side where the roles are reversed. This system is known to exhibit bulk phase separation by nucleation and growth processes or spinodal decomposition depending on the relative phase fraction.[13,14] The role of nanostructures in PbTe−PbS has been extensively analyzed and has been shown to be critical in reducing the lattice thermal conductivity.[28] Similarly, when the PbSe−PbS system (previously believed to be a solid solution) was studied with transmission electron microscopy (TEM) it was discovered that nanostructuring did occur and could be used to account for the lower than expected thermal conductivity.[19] The PbTe−PbSe system is also a high-performance thermoelectric system, but it has not been analyzed in detail from the point of view of TEM. It is believed to be a solid solution lacking nanostructuring, and its low lattice thermal conductivity has been explained on the basis of point defects created by the Te/Se mixed occupation in the rock-salt structure and by the presence of doping.[23]

Considering the latest developments in the pseudobinary systems and in the context of (a) acquiring deeper understanding of the fundamental properties of the lead chalcogenide family and (b) developing high performance materials, we investigated the pseudoternary system PbTe−PbSe−PbS. Given the altered valence band convergence of PbTe−PbSe, the purported lack of nanostructures in PbTe−PbSe, yet the proven presence of nanostructures in both PbTe-PbS and PbSe−PbS, we wanted to examine the pseudoternary system PbTe−PbSe−PbS to see if these techniques for enhancing ZT can be combined into one system.

Several key questions arise when considering this more complex system. Is the PbTe−PbSe−PbS system a solid solution or a phase-separated nanostructured assembly? For which compositions? Can the lattice thermal conductivity be lowered further in the pseudoternary system compared to the pseudobinary systems? Can higher performance be obtained from PbTe−PbSe−PbS than from the corresponding pseudobinary materials? One could argue that the pseudoternary system of PbTe−PbSe−PbS would be even more nanostructured than, for example, PbTe−PbS because of the increased compositional complexity. However, a counterargument could state that entropic reasons may push the system into a more homogeneous, atomically mixed, solid solution state. Since the PbTe−PbSe−PbS system is not well understood or investigated we have undertaken a study of it and we present here our results for p-type Na doped samples.

Because the compositional scope of the pseudoternary $(PbTe)_{1-x-y}(PbSe)_x(PbS)_y$ is very large, in this study we limited ourselves to compositions that feature equal fractions of PbSe and PbS in PbTe: $(PbTe)_{1-2x}(PbSe)_x(PbS)_x$. We find that the lattice thermal conductivity for specific compositions is very low (e.g., 0.6 W/m·K at 800 K), and as a result a much higher thermoelectric performance can be achieved in the pseudoternary system compared to the respective pseudobinary systems. Namely, we report that the Na-doped $(PbTe)_{1-2x}(PbSe)_x(PbS)_x$ $x = 0.07$ samples processed with spark plasma sintering achieve a ZT of 2 at ∼825 K. This is higher than the PbTe−PbS and PbSe−PbS systems, but surprisingly, we find that nanostructuring does not occur in the $x = 0.07$ samples nor does it seem to be a dominant feature of the strong phonon scattering we observed in $(PbTe)_{1-2x}(PbSe)_x(PbS)_x$ compositions. Instead, the strong phonon scattering seems to arise mainly from a very effective combination of point defects and scattering between grain boundaries rather than endotaxial nanostructures.

EXPERIMENTAL SECTION

Synthesis and Sample Preparation. $Pb_{0.98}Na_{0.02}Te_{1-2x}Se_xS_x$ ingots, also denoted as $(PbTe)_{1-2x}(PbSe)_x(PbS)_x$ with 2% Na, were synthesized with $x = 0.02$, 0.05, 0.07, 0.10, and 0.12. Another series of Na-free compounds with the same stoichiometries were also synthesized for optical measurements, as the vibrational modes of free carriers in samples can mask the interband transitions in mid-IR spectral region. Ingots were prepared from elemental starting materials as received from American Elements (99.99% Pb, 99.999% Te, 99.999% Se, 99.999% S, and 99.99% Na). Stoichiometric quantities were loaded into carbon-coated fused silica tubes and flame-sealed under vacuum (∼10^{-4} Torr). The materials were heated to 1000 °C over 12 h and held at 1000 °C for 5 h before cooling to room temperature over 6 h. The ingots were ground to ∼5 mm^3 and further mechanically powdered by mortar and pestle and sieved to <53 μm^3 under nitrogen. The powders were pressed into disk-shaped pellets (10 mm diameter) using spark plasma sintering (SPS) where 60 MPa of axial pressure was applied for 10 min at 550 °C under a pulsed electric current in an argon atmosphere.

XRD Characterization. Powder X-ray diffraction patterns were collected on finely ground powders for all samples on a CPS120 Inel X-ray powder diffractometer using Ni-filtered Cu Kα radiation operating at 40 kV and 20 mA. A position-sensitive detector was used in reflection geometry.

Transmission Electron Microscopy (TEM). TEM samples were prepared by traditional polishing and dimpling followed by Ar-ion milling with a liquid Nitrogen cooling stage. Images were collected using a JEOL 2100F transmission electron microscope operating at 200 kV. Extensive TEM studies utilized several types of sample preparation techniques including ion beam milling and cryogenic smashing. Ion beam milling was the most destructive for the sample, and cryogenic smashing yielded the clearest images.

Atom Probe Tomography. An ultrahigh vacuum (UHV), at a gauge pressure of 2 to 3 × 10^{-11} Torr, ultraviolet (UV) laser-assisted local-electrode atom-probe (LEAP) tomograph (LEAP 4000XSi, Cameca, Madison, WI), was employed utilizing picosecond lasers pulses with a wavelength of 355 nm, an evaporation rate (ion $pulse^{-1}$) of 2%, a pulse repetition rate of 500 kHz, and an energy $pulse^{-1}$ of 20 pJ.[30−32] LEAP tomographic specimens were prepared using a dual-beam focused-ion beam (FIB) microscope (Helios Nanolab., FEI Co., Hillsboro, OR), initially with 30 kV Ga^+ ions, followed by 5 kV Ga^+ ions and then finally 2 kV Ga^+ ions: this procedure minimizes the concentration of Ga atoms implanted in a microtip. Needle-shaped specimens with a microtip radius of ∼20 nm were fabricated using the dual-beam FIB-based lift-out method, which were attached to Si microposts on a coupon.[33] The coupon was subsequently inserted into the LEAP tomograph's UHV chamber and cooled to 25 K prior to performing pulsed laser-assisted evaporation analyses. The microtips were maintained at a positive potential, while the evaporation of ions was triggered by the picosecond UV laser pulses. The times-of-flight of

dx.doi.org/10.1021/ja4121583 | J. Am. Chem. Soc. 2014, 136, 3225−3237

the detected ions were used to produce three-dimensional (3-D) reconstructions in direct space using the program IVAS, version 3.6.3.

Electrical Properties. The pressed samples were cut and polished into parallelepipeds with dimensions approximately 3 mm × 3 mm × 10 mm. Electrical conductivity and Seebeck coefficient were measured on a Ulvac-Riko ZEM-3 system. Samples were spray coated with boron nitride spray to minimize outgassing except where needed for electrical contact with the thermocouples, heater, and voltage probes. Samples were held between two nickel electrodes and two probe thermocouples with spring-loaded pressure contacts. Graphite pads were placed between the sample surface, electrodes, and thermocouple contacts to ensure uniform contact and protect the thermocouples. A resistive heater on the lower electrode created temperature differentials of 10, 20, and 30 °C to determine the Seebeck coefficient. Seebeck and electrical conductivity measurements were made under 0.1 atm of helium and were collected from room temperature to 825 K. The measurement error for thermopower is ∼5% and less than 5% for electrical conductivity.

Carrier concentration (n) was determined by Hall effect measurements, at room temperature, using the same parallelepipeds as for Seebeck measurements. Hall coefficients were measured in a home-built system by placing the parallelepiped with a four-contact Hall bar geometry in a magnetic field from 0.5 to 1.25 T. Measurements were taken for both magnetic field directions to eliminate voltage probe misalignment effects as well as magnetoresistance contributions. The carrier concentration was calculated assuming $R_h = 1/ne$, and mobility (μ) was calculated from $\mu = \sigma/ne$ where e is the electron charge.

Thermal Properties. A Netzsch LFA 457 Microflash was used to measure the thermal diffusivity of the SPS samples. Square parallelepipeds approximately 2 mm × 10 mm × 10 mm in dimension were coated with graphite prior to measurement. Total thermal conductivity was calculated from $\kappa_{tot} = DC_p\rho$, where D is the thermal diffusivity, C_p is the heat capacity, and ρ is the mass density of the specimens. The density was rounded 8.1 g/cm^3 for all samples (Table S1, Supporting Information). The densities of all samples measured by an AccuPyc 1340 were greater than 98% theoretical density and ranged from 8.05 to 8.11 g/cm^3. The specific heat of the $(PbTe)_{1-2x}(PbSe)_x(PbS)_x$ alloy was determined by a weighted average of the temperature-dependent specific heat literature values for PbTe, PbS, and PbSe.[34,35]

Infrared Optical Properties. Room-temperature diffuse reflectance spectra of Na-free compositions were performed on finely ground powders to probe the optical energy gap. The spectra were collected in the mid-IR range (6000−400 cm^{-1}) using a Nicolet 6700 FTIR spectrometer. Absorption data (a/S) were calculated from reflectance data via the Kubelka−Munk transformation.[36]

Electronic Structure Calculations. Density functional theory (DFT)[37,38] calculations were performed using the Vienna Ab initio Simulation Package (VASP)[39] using projector-augmented wave (PAW)[40] potentials and the generalized gradient approximation (GGA) of Perdew, Burke, and Ernzerhof (PBE)[41] for the exchange-correlation functional. Calculations were carried out using plane-wave basis sets with cutoff energies of 350 eV, k-point sampling was performed with Monkhorst-Pack[42] meshes containing k-point densities of 2400 k-points per reciprocal atom (KPPRA), and Brillouin zone integrations were carried out using Gaussian smearing of electronic occupancies with a 0.1 eV smearing width. These settings yield DFT formation enthalpies which are converged to within 1 meV/cation with respect to cutoff energies and k-point meshes.[43]

RESULTS AND DISCUSSION

Structural Characterization (X-ray, Bandgap, Miscibility Calculations). Despite the recent prominence of PbTe PbSe, and PbS in the thermoelectrics literature, the combined quaternary (or pseudoternary) PbTe−PbSe−PbS system is relatively unexplored. The phase relations between PbTe−PbSe−PbS have been reported be a complete solid solution along the PbSe−PbS line, while a miscibility gap exists along the PbTe−PbSe and PbS−PbTe lines as a function of temperature and composition.[44] Several reports have investigated the role of impurities on the electron and phonon scattering in n-type PbTe−PbSe−PbS materials.[45] No significant variations of the energy dependence of the mechanism of scattering were found compared to PbTe, and there is an additive effect of Se and S atoms upon the scattering of electrons up to 10 atomic % concentration of impurity centers.[45] The thermoelectric properties and figure of merit for various compositions of n-type $(PbTe)_{1-2x}(PbSe)_x(PbS)_x$ samples were investigated between 77 to 300 K, and reported a max ZT of 0.6 for $(PbTe)_{0.80}(PbSe)_{0.10}(PbS)_{0.10}$.[46] However, the structure and properties of p-type $(PbTe)_{1-2x}(PbSe)_x(PbS)_x$ have not been previously reported and are described in detail herein.

Experimental powder X-ray diffraction patterns for selected samples are given in Figure 1 for $(PbTe)_{1-2x}(PbSe)_x(PbS)_x$

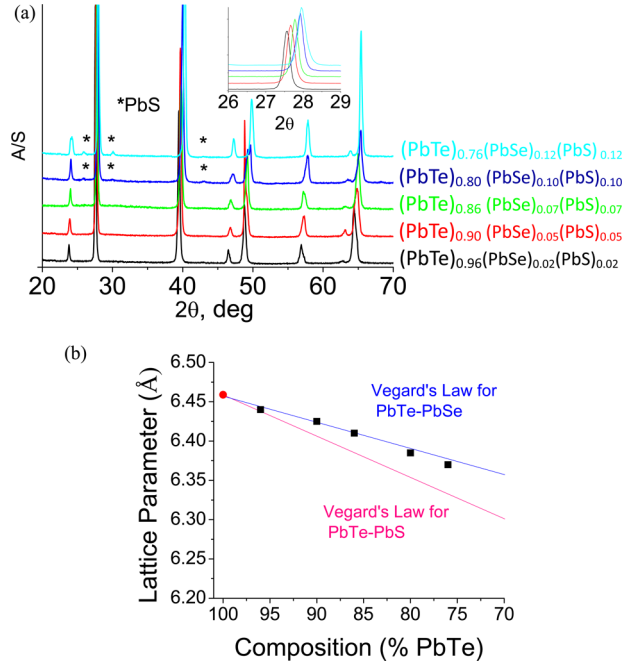

Figure 1. (a) Powder X-ray diffraction data for 2% Na doped $(PbTe)_{1-2x}(PbSe)_x(PbS)_x$ samples. PbS peaks appear for samples with more than 7% PbS. (b) The lattice parameter is plotted against % PbTe. The lattice parameter decreases in general accordance with Vegard's law mixtures for PbTe−PbSe rather than PbT−-PbS.

compositions. Because of the very large number of compositions in the system of $(PbTe)_{1-x-y}(PbSe)_x(PbS)_y$ we limited out present study to a select few which we felt represented well the phase space where the relevant issues could be studied while keeping PbTe to be the majority (matrix) phase. For simplicity, we kept the fractions of PbSe and PbS equal.

As can be seen from Figure 1, simultaneous alloying with Se and S results in lattice contraction, i.e., shifting of the PbTe Bragg peaks to higher 2θ angles. The x = 0.02, 0.05, and 0.07 compositions are macroscopically single phase, whereas for higher x values additional reflections are observed attributed to PbS precipitation. The determined lattice parameters shown in Figure 1b were found to decrease on increasing sulfur and selenium content, which is consistent with the increasing incorporation of the smaller S and Se atoms in the lattice. The lattice parameter values lie closer to the expected Vegard's law

dx.doi.org/10.1021/ja4121583 | J. Am. Chem. Soc. 2014, 136, 3225−3237

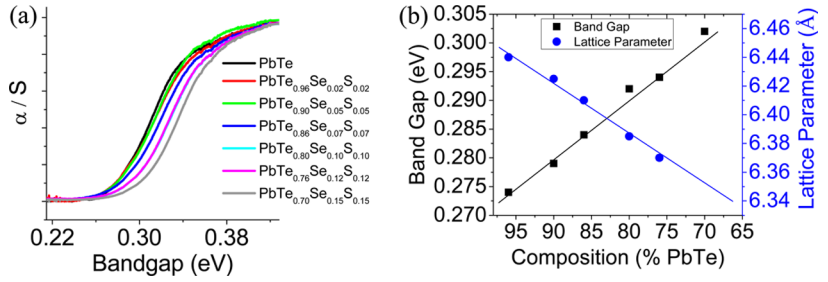

Figure 2. (a) Bandgap shifts to higher energy with increasing amounts of PbSe/PbS alloying. No sodium dopant was added in order to minimize interband states. (b) Bandgap and lattice parameter as a function of PbTe alloy composition. The lattice parameter decreases and the bandgap increases with increasing PbSe and PbS content, which is consistent with PbSe/PbS incorporation.

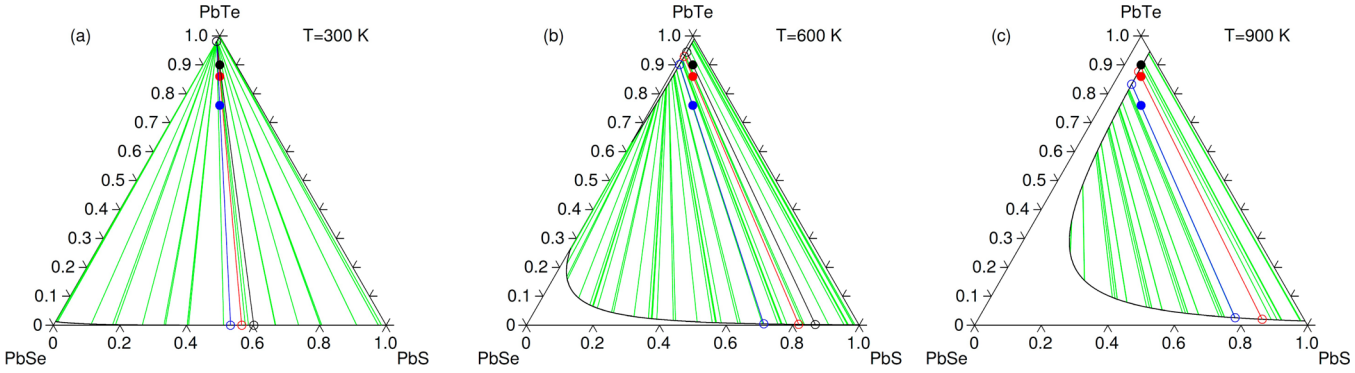

Figure 3. Pseudoternary isothermal sections of the $(PbTe)_{1-x-y}(PbSe)_x(PbS)_y$ phase diagram calculated using DFT energetics at temperatures of (a) 300 K, (b) 600 K, and (c) 900 K. Single-phase boundaries are shown in black, and tie-lines are shown in green. At each temperature, alloy compositions of $(PbTe)_{0.90}(PbS)_{0.05}(PbSe)_{0.05}$, $(PbTe)_{0.86}(PbS)_{0.07}(PbSe)_{0.07}$, and $(PbTe)_{0.76}(PbS)_{0.12}(PbSe)_{0.12}$, are plotted as solid black, red, and blue circles, respectively. The equilibrium matrix and precipitate compositions corresponding to each alloy composition are shown as open circles connected by tie-lines of the same color as the alloy composition.

for the pseudobinary system $(PbTe)_{1-x}(PbSe)_x$ than to the $(PbTe)_{1-x}(PbS)_x$ system indicating a higher solubility of Se in PbTe while PbS tends to phase separate. In the PbSe/PbS-rich compositions $x = 0.10$, 0.12 we observe PbS as a second phase. Closer inspection of the minor phase PbS Bragg peaks in the $(PbTe)_{0.76}(PbSe)_{0.12}(PbS)_{0.12}$ diffraction patterns gives a lattice parameter of 5.954(3) Å which is slightly expanded from 5.936 Å of pristine PbS. The larger lattice parameter suggests some incorporation of larger Se or Te atoms into the PbS rich precipitate phase.

To further determine the influence of the incorporation of Se and S into the PbTe matrix, the room-temperature electronic absorption spectra of several Na-free $(PbTe)_{1-2x}(PbSe)_x(PbS)_x$ samples were measured, within the range 0.2−0.5 eV, are shown in Figure 2a. As can be seen from Figure 2a, the absorption lines shift to higher energies with increasing PbS and PbSe content. The obtained band gaps as a function of composition shown in Figure 2b increase from 0.276 eV for PbTe to 0.304 eV for $(PbTe)_{0.70}(PbSe)_{0.15}(PbS)_{0.15}$. The room-temperature band gaps for PbTe and PbSe are similar at ∼0.3 and ∼0.28 eV, respectively, while PbS has a larger band gap around 0.4 eV at room temperature. Since Se incorporation would be expected to slightly reduce the band gap, the observed increase is attributed to the incorporation of S in the lattice. Considering a $(PbTe)_{1-2x}(PbSe)_x(PbS)_x$ alloy and approximating the band gap of the solid solution as a composition-weighted average of the band gaps of PbTe, PbSe, and PbS, one would expect a band gap value at ∼0.313 eV for $x = 0.3$ (70% PbTe), slightly higher than the observed ∼0.304 eV of Figure 2b. Although a small reduction in the band gap may be attributed to Se incorporation into PbTe, this deviation more likely denotes that not all of the S is dissolved within the matrix, which is further supported by the emergence of the PbS rich peaks observed in the PXRD spectra of Figure 1.

Despite the previous reports on these pseudobinary and pseudoternary systems, there remains considerable uncertainty as to the extent of mixing or phase separation in lead chalcogenides alloys. For example, PbTe−$AgSbTe_2$ and SnTe−$AgSbTe_2$ were thought to be solid solutions but found to be inhomogeneous on the nanoscale.[1,47,48] Similarly, $(PbSe)_{1-x}(PbS)_x$ was reported to be a solid solution below 1060 °C; however, nanostructuring was later observed with TEM imaging.[19,49−51] On the other hand $(PbTe)_{1-x}(PbS)_x$ is known to exhibit regions of solid solution, spinodal decomposition, or nucleation and growth according to the composition and temperature.[13] To better understand the solubility of these systems, theoretical phase diagrams were calculated using DFT for the pseudoternary $(PbTe)_{1-x-y}(PbSe)_x(PbS)_y$ isothermal sections at 300, 600, and 900 K.

The calculated pseudobinary phase diagrams of $(PbSe)_{1-x}(PbS)_x$, $(PbTe)_{1-x}(PbSe)_x$, and $(PbTe)_{1-x}(PbS)_x$ show incoherent phase separation containing miscibility gaps with maximum temperatures of 275 K, 630 K, and 1770 K for $(PbSe)_{1-x}(PbS)_x$, $(PbTe)_{1-x}(PbSe)_x$, and $(PbTe)_{1-x}(PbS)_x$, respectively.[43] Though these calculated miscibility gaps overestimate the experimentally determined miscibility gap temperatures, they are still useful for understanding trends and estimating pseudoternary miscibility gap temperatures.

dx.doi.org/10.1021/ja4121583 | J. Am. Chem. Soc. 2014, 136, 3225−3237

Several isothermal sections of the pseudoternary system are shown in Figure 3. In the system $(PbTe)_{1-x-y}(PbSe)_x(PbS)_y$, below any of the pseudobinary maximum miscibility gap temperatures there exists a three-phase equilibrium between PbTe-, PbSe-, and PbS-rich phases. Above the maximum miscibility gap temperature of $(PbSe)_{1-x}(PbS)_x$ (275 K), the three-phase region disappears and the two-phase equilibria in the $(PbTe)_{1-x}(PbSe)_x$ and $(PbTe)_{1-x}(PbS)_x$ pseudobinary systems extend into the ternary composition space and connect with one another (Figure 3a,b). This two-phase region is a miscibility gap between a PbTe-rich phase and a $(PbSe)_{1-x}(PbS)_x$ rich phase. Above the maximum miscibility gap temperature of $(PbTe)_{1-x}(PbSe)_x$ (630 K), the two-phase region of $(PbTe)_{1-x}(PbS)_x$ extends into the ternary composition space but does not connect with the $(PbTe)_{1-x}(PbSe)_x$ pseudobinary edge (Figure 3c). From this discussion we can conclude that phases formed from a PbTe-rich alloy in $(PbTe)_{1-x-y}(PbSe)_x(PbS)_y$ above room temperature should be PbSe−PbS−rich phases in a PbTe-rich matrix.

Taken together, the Na-doped $(PbTe)_{1-2x}(PbSe)_x(PbS)_x$ samples exhibit mainly solid solution behavior. The presence of a few large PbS-rich precipitates >100 nm (not shown) is supported by X-ray diffraction and theoretical calculations. The behavior of these large precipitates at high temperature has not been characterized, but they are not expected to contribute significantly in the reduction of the κ_{latt} component based on their size. Phonons with mean free paths smaller than 10 nm comprise around 90% of the lattice thermal conductivity for PbTe.[52] Therefore, to significantly reduce the lattice thermal conductivity in these materials, nanostructures with characteristic length smaller than ∼20−30 nm are required. The PbS precipitates observed are much larger than the mean free path of the heat carrying phonons and are not expected to contribute to phonon scattering and reductions in κ_{latt}. These observations are consistent with the κ_{latt} values observed in the system, which are discussed in detail below. Initial calculations confirm the κ_{latt} values observed in the Na-doped $(PbTe)_{1-2x}(PbSe)_x(PbS)_x$ system are consistent with solid solution alloy behavior. Future studies may explore the formation, solubility, and transport effects of these PbS-rich precipitates.

Electrical Transport Properties. Table 1 presents the room-temperature electrical conductivity, hole carrier concentration, and the hole mobility of the studied compositions. The carrier concentration for all samples is $\sim 1 \times 10^{20}$ cm^{-3}, since the Na doping fraction is fixed at 2%, denoting heavily doped compositions. Na doping has been shown to not significantly alter the band structure while providing sufficient acceptor states for high hole concentrations and high power factors.[25,12,53−55] The room-temperature electrical conductivity decreases with increasing PbSe and PbS content. This reflects the decreased mobility, probably due to scattering from the increased atomic disorder alloying.

Table 1. Conductivity, Hole Carrier Concentration, and Mobility at Room Temperature for 2% Na-Doped $(PbTe)_{1-2x}(PbSe)_x(PbS)_x$[a]

sample	σ (S/cm)	carriers (cm^{-3})	mobility (cm^2/(V s))
x = 0.02	2625	1.07×10^{20}	153
x = 0.05	2138	0.973×10^{20}	137
x = 0.07	1908	1.01×10^{20}	118
x = 0.01	1623	1.05×10^{20}	96

[a]Since the carrier concentration is approximately constant, the mobility decreases with decreasing σ.

The room-temperature Seebeck coefficient shows similar values for all the studied compositions. A Pisarenko plot of the Seebeck coefficient vs hole carrier density is shown in Figure 4

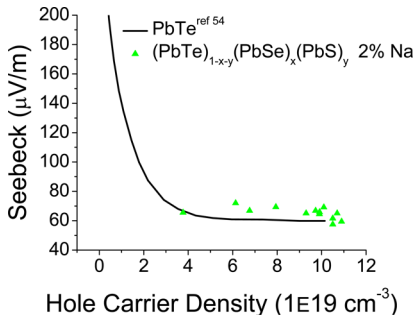

Figure 4. Two-band theoretical model for PbTe Pisarenko relation is plotted. Experimental points for varying compositions of 2% Na doped $(PbTe)_{1-x-y}(PbSe)_x(PbS)_y$ samples fall near the expected Seebeck coefficient values for PbTe within the error of the effective mass. No enhancement from resonance scattering is observed. The theoretical solid line for PbTe is from ref 54.

together with the theoretical line calculated based on a two-band model for p-type PbTe.[7,54] In heavily doped p-type PbTe it is important to consider effects of the light hole band (LHB) at the L point of the Brillouin zone with density of states mass m_l* and the heavy hole band (HHB) at the Σ point with density of states mass m_h*. The presence of the second sub-band manifests itself by the constant values of thermopower in the high carrier density range. The theoretical line of Figure 4 is obtained taken m_h* = 1.2 m_o and m_l* = 0.36 m_o and includes a band gap $\Delta E \approx 0.12$ eV between the valence sub-bands at room temperature.[54] The experimental data points found lying on the high carrier density side of the theoretical line suggest the room temperature Fermi level lies deep in the valence band and a significant contribution of the HHB to the Seebeck coefficient. The experimental Seebeck values are slightly above the theoretical values, probably due to a slightly higher effective mass. Based on the Pisarenko plot in Figure 4, it is clear the HHB contributes to the thermopower. This is consistent with the heavy valence band involvement reported previously[7,56,57] and does not indicate any enhancement of the Seebeck values due to resonance scattering.[18,19]

As shown in Figure 5a,b, there is a noticeable flattening of the electrical conductivity and the Seebeck coefficient beginning at 600 K. The observation of plateau behavior in the hole Seebeck coefficient at high temperatures has been reported previously in PbTe and $(PbTe)_{1-x}(PbS)_x$.[12,54] Figure 6 compares the Seebeck values of p-type PbTe, $(PbTe)_{0.86}(PbSe)_{0.07}(PbS)_{0.07}$, $(PbTe)_{0.88}(PbS)_{0.12}$, and $(PbTe)_{0.75}(PbSe)_{0.25}$. For p-type PbTe, the plateau region was attributed to the contribution from carriers of the opposite sign negating the increase in Seebeck from HHB contributions seen from 300 to 700 K.[54] The initial proposition of intrinsic electrons causing the plateau is suspect since the number of intrinsic negative carriers in similarly doped materials is reported to be $\sim 10^{16}$ cm^{-3} at 500 K, which is too low to create such a pronounced effect on the Seebeck coefficient with an extrinsic hole concentration $\sim 10^{20}$ cm^{-3}.[58,59] Recent research on the temperature dependence of the valence band structure of PbTe and $(PbTe)_{1-x}(PbS)_x$ alloys reported

dx.doi.org/10.1021/ja4121583 | J. Am. Chem. Soc. 2014, 136, 3225−3237

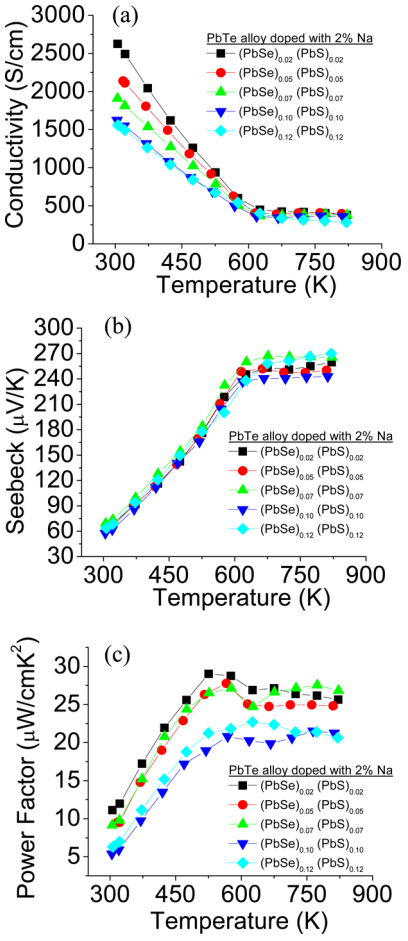

Figure 5. (a) Electrical conductivity, (b) Seebeck coefficient, and (c) power factor of 2% Na-doped $(PbTe)_{1-2x}(PbSe)_x(PbS)_x$ alloyed materials upon heating. A sharp transition is observed at 600 K for the electrical conductivity and Seebeck coefficient. Instead of monotonic behavior upon cooling, from 600 to 825 K a plateau is observed.

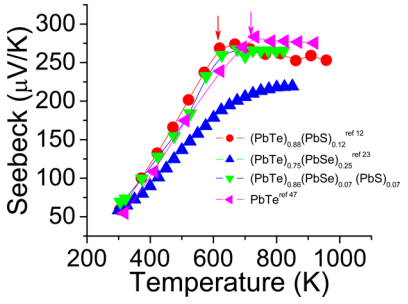

Figure 6. Comparison of Seebeck coefficient values for different lead chalcogenide systems. The PbS-containing compositions show higher Seebeck values in the 400−600 K temperature range accompanied by a plateau which is onset (shown with arrows) and shifted to lower temperatures relative to the PbTe single crystal of Airapetyants et al.[54]

negatively sloped Hall coefficient data with applied magnetic field at around 620 K suggesting the presence of topological electrons on the order of $\sim 10^{19}$ cm^{-3}.[59] The origin of the electron-like behavior at high temperature was attributed to the topology of the band structure. For high doping levels the LHB and HHB are singly connected through a continuous Fermi surface giving rise to regions of negative curvature.[53,59,60] These regions respond as electrons showing negative Seebeck values, and they begin to contribute negatively to the absolute value of the Seebeck coefficient as the temperature is increased to ≈600 K and above. At this temperature range they are located within a few k_BT of the Fermi level, giving rise to the saturation of the thermopower and electrical conductivity.[59]

Curiously, the conductivity and thermopower measurements show different behavior on heating and cooling in the high temperature range around 650 K. Figure 7 shows the measured

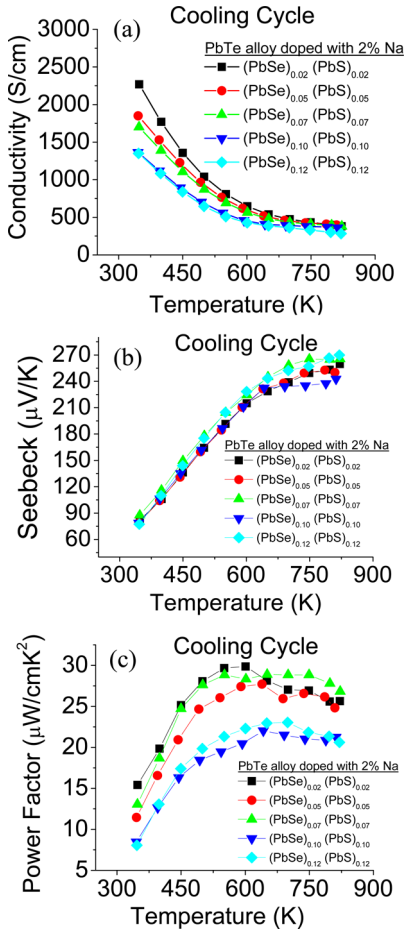

Figure 7. (a) Electrical conductivity, (b) thermopower, and (c) power factor of 2% Na-doped $(PbTe)_{1-2x}(PbSe)_x(PbS)_x$ alloyed materials upon cooling. The cooling data decrease monotonically for the electrical conductivity and increase for the Seebeck. The highest power factor is observed in $(PbTe)_{0.86}(PbSe)_{0.07}(PbS)_{0.07}$.

electrical conductivity, Seebeck coefficient, and thermopower versus temperature for the 2% Na $(PbTe)_{1-2x}(PbSe)_x(PbS)_x$ samples upon cooling from high temperature. The trend upon cooling shows a smooth and monotonically decreasing behavior, similar to other PbTe systems. However, during the heating cycle, shown in Figure 6, the conductivity decreases linearly from 300 to 600 K while the thermopower increases linearly. At 600 K however a sharp break in the linearity in both properties is observed. At higher temperatures, the thermopower and electrical conductivity reach a plateau from 650 to 800 K. When cooling, the sharp break seen in the Seebeck coefficient and electrical conductivity observed upon heating is not observed around 650 K and the conductivity values of the same sample are slightly higher and Seebeck coefficient values slightly lower than the heating cycle (see Figure S1, Supporting Information). However, above 700 K the conductivity and

dx.doi.org/10.1021/ja4121583 | J. Am. Chem. Soc. 2014, 136, 3225−3237

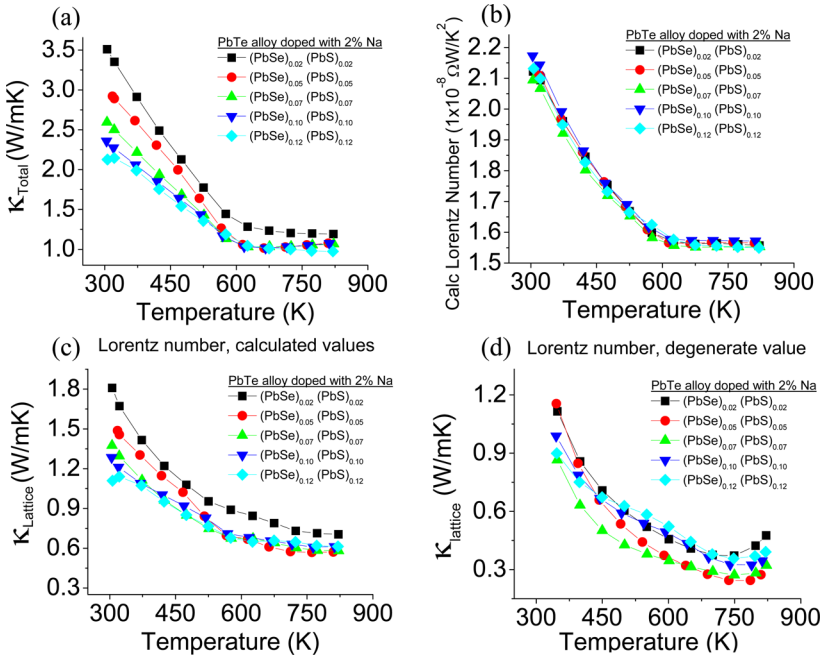

Figure 8. (A) Total thermal conductivity, (b) calculated Lorenz numbers from a single parabolic model Fermi integral calculation using data from the heating cycle, (c) lattice thermal conductivity calculated from the single parabolic model, and (d) lattice thermal conductivity calculated from the Sommerfeld value of $L_o = 2.45 \times 10^{-8}$ ΩW/K^2 of 2% Na-doped $(PbTe)_{1-2x}(PbSe)_x(PbS)_x$ alloyed materials.

Seebeck coefficient are the same for heating and cooling and do not adversely affect the maximum of the power factor. Upon cooling, the power factor reaches and maintains a very high value of ~27 μW/cmK^2 between 600 and 800 K for $(PbTe)_{0.86}(PbSe)_{0.07}(PbS)_{0.07}$ as seen in Figures 5c and 6c. The lowest power factor in this system is still very high, reaching ~20 μW/cmK^2 between 600 and 800 K for $(PbTe)_{0.76}(PbSe)_{0.12}(PbS)_{0.12}$. The reason for the different behavior during the two cycles is not yet clear and one may suppose that this situation is related to structural changes taking place, possibly including the dissolution of excess Na^+ into the matrix.[10,14] Further studies are needed to better understand this effect.

Comparing the onset temperature of the saturation of the Seebeck coefficient between the PbTe and the PbTe–PbS compositions of Figure 7, it is obvious that the saturation onset of the PbS containing samples is located at a lower temperatures than the pristine PbTe sample. This may be attributed to the fact that sulfur p orbitals lower the energy of the LHB, i.e., increasing the band gap as shown in Figure 2. By lowering the LHB, the electron-like regions are closer to the Fermi energy and start to contribute to the Seebeck coefficient at lower temperatures compared to pure PbTe. The fact that the S incorporation is related to the Seebeck plateau formation (Figure 5) is further supported by the absence of this behavior in the Na doped $(PbTe)_{1-x}(PbSe)_x$ compositions. Given that the band gap of PbSe is slightly narrower than that of PbTe,[61] we expect that Se alloying does not lower the energy of the LHB and thus the contribution of the negative curvature regions of the Fermi surface, with rising temperature, remains unaffected or even delayed.

Thermal Conductivity and Figure of Merit. The total thermal conductivity (κ_{tot}) as a function of temperature is shown in Figure 8a. The room temperature κ_{tot} values decrease with increasing amounts of PbSe and PbS. At high temperatures, the values reach ~1.1 W/m·K for the x = 0.5–0.10 samples. The x = 0.12 sample is slightly lower at ~1.0 W/m·K . The addition of the PbSe and PbS contribute to a 30% reduction in κ_{tot} at high temperature over that of pristine PbTe.[12] These low values coupled with the high power factors give rise to exceptional values of ZT. Figure 9 presents the

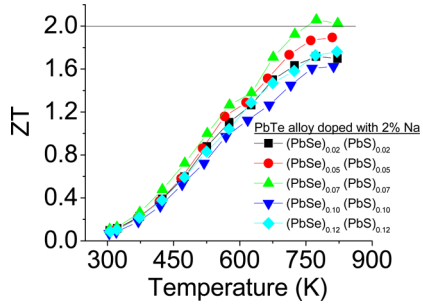

Figure 9. ZT of 2% Na-doped PbTe and PbTe–PbSe–PbS alloyed materials. $(PbTe)_{0.86}(PbSe)_{0.07}(PbS)_{0.07}$ reaches ZT of 2.0 at 825 K.

temperature dependent ZT values of different 2% Na-doped $(PbTe)_{1-2x}(PbSe)_x(PbS)_x$ samples. The $(PbTe)_{0.86}(PbSe)_{0.07}(PbS)_{0.07}$ composition achieved the highest $ZT \approx 2.0$ at 823 K by combining high power factor values of 27 μW/cm·K^2 with a κ_{tot} of 1.1 W/m·K. $(PbTe)_{0.90}(PbSe)_{0.05}(PbS)_{0.05}$ also achieved a high ZT of 1.8 at 825 K. The x = 2% sample achieved a high power factor, similar to x = 7%, but the κ was higher giving an overall $ZT \approx 1.6$ at 825 K. Likewise, the x = 10, 12 samples had low thermal conductivity but the lower power factor resulted in $ZT \approx 1.5$ for both samples.

These low total thermal conductivity values imply a very low lattice thermal conductivity. The lattice thermal conductivity was determined by subtracting κ_{el} from the Wiedemann–Franz relation $\kappa_{el} = LT\sigma$ from κ_{tot} such that $\kappa_{latt} = \kappa_{tot} - LT\sigma$ where L is the Lorentz number, T is temperature, and σ is electrical conductivity. In the present case, great care must taken on

dx.doi.org/10.1021/ja4121583 | J. Am. Chem. Soc. 2014, 136, 3225–3237

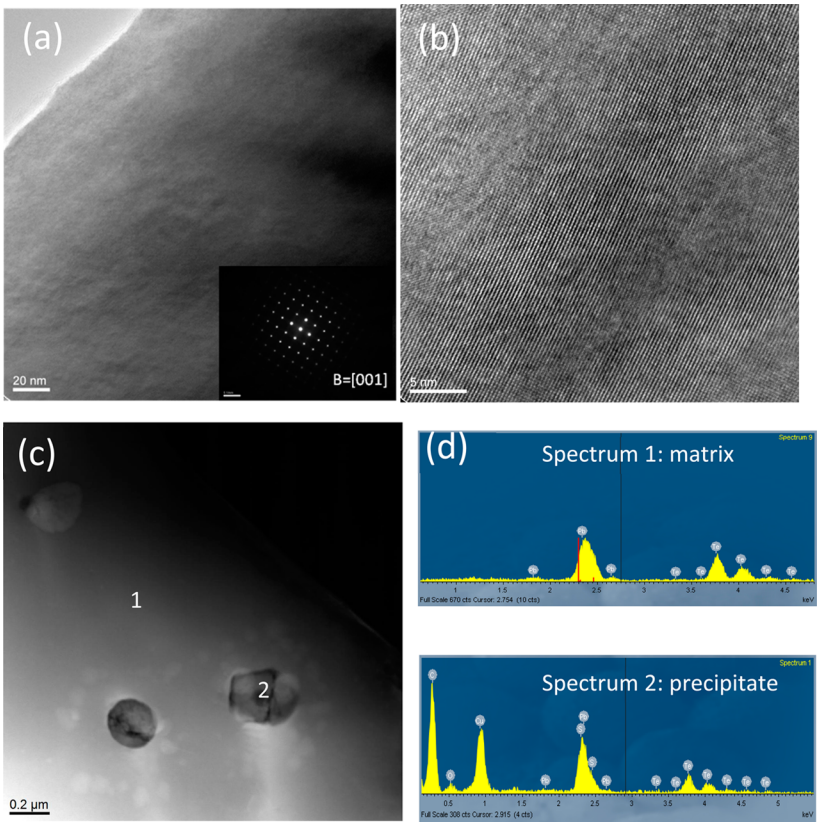

Figure 10. TEM images $(PbTe)_{0.86}(PbSe)_{0.07}(PbS)_{0.07}$. (a) Low magnification image shows homogeneous material. Inset shows the corresponding SAD. (b) High magnification image indicates the single-crystal lattice. (c) The Z-contrast image shows the existence of the large precipitate, and the corresponding EDS spectra are shown in (d). The C, Cu, and O peaks in spectrum 2 are from the TEM grid underneath the sample.

estimating the Lorentz number. There are two limiting values for L, the Sommerfeld value of $L_{DEG} = 2.45 \times 10^{-8}$ $\Omega W/K^2$, which is valid for metals and highly degenerated electron gas, and the value for the nondegenerate limit $L_{N-D} = 1.49 \times 10^{-8}$ $\Omega W/K^2$. Clearly, the former value overestimates the electronic contribution to thermal conductivity, while the later one underestimates it. In a single band parabolic model when only one type of carriers is present, L is easily calculated. We will return to this issue below when discussing the calculation of κ_{latt}. The Lorentz number can be estimated based on the Seebeck coefficient measurements and assuming scattering from acoustic phonons, following the equations from the Fermi–Dirac statistics

$$S = \pm\frac{k_B}{e}\left[\frac{2F_1(\eta)}{F_0(\eta)} - \eta\right] \quad (1)$$

$$L = \left(\frac{k_B}{e}\right)^2\left[\frac{3F_0(\eta)F_2(\eta) - 4F_1^2(\eta)}{F_0^2(\eta)}\right] \quad (2)$$

$$F_i(\eta) = \int_0^\infty \frac{x^i dx}{1 + \exp(x - \eta)} \quad (3)$$

where η is the reduced Fermi energy (E_F/k_BT), $F_i(\eta)$ the Fermi–Dirac integrals, and k_B the Boltzmann constant. However, due to the complexity and nonparabolicity of the valence band structure around the Fermi level for p-type PbTe, a more accurate determination of the Lorenz number is difficult, though it can be roughly estimated using a single parabolic band (SPB) model with acoustic phonon scattering.[57] The calculated L values for all samples are shown in Figure 8b. As can be seen, in the entire temperature range the Lorenz numbers are well below the Sommerfeld value of L_{DEG} and above the nondegenerate limit.

Figure 8c gives the lattice thermal conductivity calculated with the L values for the SPB model. The lattice thermal conductivity values are strongly reduced by 50–60% compared with PbTe.[12] The lowest lattice thermal conductivity is observed in $(PbTe)_{0.90}(PbSe)_{0.05}(PbS)_{0.05}$ with κ_{latt} = 0.5 W/m·K at 825 K. The alloy compositions greater than $x = 0.05$ are also very low with values around 0.6 W/m·K. The smallest reduction of κ_{latt} =0.7 W/m·K is observed at 800 K in the $(PbTe)_{0.96}(PbSe)_{0.02}(PbS)_{0.02}$ sample, most likely due to the lowest alloy composition. However, a significant reduction compared to PbTe is still observed with only 4% alloying on the Te site.

Similar low lattice thermal conductivities have been reported in lead chalcogenide systems such as the nanostructured systems $Na_{0.95}Pb_{20}SbTe_{22}$, PbTe–2%SrTe, and $(PbTe)_{1-x}(PbS)_x$ system.[5,13,15] Therefore, we investigated the high ZT Na-doped $(PbTe)_{1-2x}(PbSe)_x(PbS)_x$ samples for the presence of nanoparticles using TEM characterization. Figure 10 shows an image of the matrix of 2% Na-doped $(PbTe)_{0.86}(PbSe)_{0.07}(PbS)_{0.07}$. The low magnification image of $(PbTe)_{0.86}(PbSe)_{0.07}(PbS)_{0.07}$ doped with 2% Na in Figure 10a shows a homogeneous matrix. The corresponding selected area electron diffraction pattern (SAED) along the [001] direction, shown in the inset, also illustrates the single crystal nature of the sample and its rock-salt NaCl type structure. Figure 10b is the high magnification image showing a clean single crystal and the

dx.doi.org/10.1021/ja4121583 | J. Am. Chem. Soc. 2014, 136, 3225–3237

absence of any small second phases. However, a few large ∼100−200 nm particles were observed as shown in Figure 10c. The elemental composition of the matrix and these precipitates was investigated by EDS. By comparing the EDS spectrum 1 and spectrum 2 in Figure 10d, which were collected from the matrix and the precipitate respectively, it is shown that the sulfur is aggregated at the large precipitate labeled 2 in Figure 10c. The EDS spectrum 1 lacks the front shoulder on the Pb peak indicating very little S appears to be present in the matrix. Exact quantification of the amount of sulfur is difficult due to the close proximity of the Pb $M\alpha_1$ and S $K\alpha_1$ emission energies at 2.34 and 2.31 keV, respectively. However, from qualitative analysis, the precipitates are more sulfur-rich than the matrix, which suggests the precipitates are PbS, consistent with the powder X-ray diffraction data and the calculated phase diagrams.

To study the composition of the matrix in greater detail, LEAP tomography was employed to analyze it on an atomic scale. A volume of the $(PbTe)_{0.86}(PbSe)_{0.07}(PbS)_{0.07}$ sample was analyzed ($90 \times 90 \times 600$ nm^3), which contained 25746245 atoms. LEAP tomography yields the compositions of subnanoscale solute clusters, nanoscale precipitates, and solute excesses at interfaces.[62−65] LEAP tomography achieves a true 3-D atomic-scale analysis by using picosecond UV laser pulses to remove individual atoms from a microtip's surface, essentially one atom at a time. A position-sensitive detector (microchannel plate) plus a delay-line detector are used in series to determine the chemical identity of each evaporated ion by time-of flight mass spectrometry, which yields the ratio of mass to charge state of each ion detected, and its position in 3-D direct space, respectively.

The results of a LEAP tomographic analyses of the matrix are presented in Table 2 for a sample with the overall composition

Table 2. LEAP Tomographic Elemental Analysis Results for $(PbTe)_{0.86}(PbSe)_{0.07}(PbS)_{0.07}$

element	concentration (atomic %)	LEAP tomographic results (atomic %)
Pb	49.0	51.1 ± 0.031
Te	43.0	40.8 ± 0.026
Se	3.5	4.2 ± 0.0074
S	3.5	2.4 ± 0.0055
Na	1.0	1.5 ± 0.0044

$(PbTe)_{0.86}(PbSe)_{0.07}(PbS)_{0.07}$. Given the nominal composition of 3.5 at.% S, LEAP tomography detected 2.4 atomic % S in the matrix. All the semiconducting thermoelectric systems, we have studied and are studying, are not at thermodynamic equilibrium and therefore it is not surprising that we do not obtain exact stoichiometric ratios for the different semiconducting phases. This question can best be answered experimentally in the long run by performing aging experiments at constant aging temperatures, performing isothermal experiments, and observing how the compositions of the precipitate phases evolve temporally as well as how the composition of the matrix evolves with time. More LEAP tomographic analyses are required to establish whether or not a decreased sulfur concentration in the matrix is real, but current results seem to indicate that not all the sulfur ends up in the matrix, as also observed in the TEM. While we cannot completely rule out the presence of small nanostructures, the LEAP tomographic studies could find no evidence of them.

Despite the absence of evidence for small nanostructures, 2% Na-doped $(PbTe)_{1-2x}(PbSe)_x(PbS)_x$ samples do possess very low thermal conductivities. At room temperature, the reduction in κ_{tot} follows the reduction in electronic mobility more than the reduction of κ_{latt}. Mass contrast between the three different chalcogenide atoms introduces extra sources of strain compared to a two component alloy.

Alloying PbTe with PbSe and PbS, reduces the lattice thermal conductivity of PbTe by introducing point defects which scatter phonons. If the phonon scattering from endotaxial interfaces is further negligible, as is the case for materials without nanostructuring, one may assume that the only existing phonon scattering mechanism in solid solutions would be the Umklapp and the point defect scattering. Klemens has proposed the following relation between $\kappa_{latt,alloy}$ and that of the pure compound $\kappa_{latt,pure}$[66]

$$\kappa_{latt,alloy} = \kappa_{latt,pure}\frac{\tan^{-1}(u)}{u},\ u^2 = \pi\frac{\Theta_D\Omega}{2\hbar v^2}\kappa_{latt,pure}\Gamma$$
$$\Gamma = x(1-x)\left[\left(\frac{\Delta m}{m}\right)^2 + \varepsilon\left(\frac{\Delta\alpha}{\alpha}\right)^2\right] \quad (4)$$

where Θ_D is the Debye temperature, Ω is the molar volume, v is the velocity of sound, and the Γ is a disorder scaling parameter that depends on mass and strain field fluctuations ($\Delta m/m$ and $\Delta\alpha/\alpha$). This expression has been successfully used by Wang et al.[67] to show that the PbTe−PbSe system forms solid solution (experimental κ_{latt} is well described by the theoretical one) and by Androulakis et al. to demonstrate nanostructuring in the PbSe−PbS system[19] (experimental κ_{latt} values are lower than the theoretically predicted ones). Abeles extended the formula by Klemens, taking into account not only Umklapp and point defect scattering but also phonon scattering by a normal process[68]

$$\kappa_{latt,alloy} = \kappa_{latt,pure}\left(\frac{1}{1+\frac{5a}{9}}\right)\left[\frac{\tan^{-1}u}{u} + \frac{1-\left(\frac{\tan^{-1}u}{u}\right)^2}{\frac{1+a}{a}\left(\frac{u^4}{5}-\frac{u^2}{3}-\frac{\tan^{-1}u}{u}+1\right)}\right] \quad (5)$$

where α is the ratio of normal-to-Umklapp process. Zaitsev et al.[69] have used the Abeles expression for the Mg_2Si−Mg_2Ge system and concluded that the lattice thermal conductivity is better described with the ratio of normal-to-Umklapp process should be $\alpha = 1$. Adachi[70] simplified the Klemens and Abeles expression, introducing a bowing factor (C_{B-C})

$$W(x) = \frac{1}{\kappa(x)} = xW_{AB} + (1-x)W_{AC} + x(1-x)C_{B-C} \quad (6)$$

where W_{AB} and W_{AC} are the thermal resistance for the two end members. Later, Adachi[71] expanded eq 6 for quaternary alloys ($AB_XC_YD_Z$) as

dx.doi.org/10.1021/ja4121583 | J. Am. Chem. Soc. 2014, 136, 3225−3237

$$W(x, y, z) = \frac{1}{\kappa(x, y, z)} = xW_{AB} + yW_{AC} + zW_{AD} + xyC_{BC} + yzC_{CD} + zxC_{DB}$$
$$\text{with } x + y + z = 1 \quad (7)$$

In our case, for pseudoternary $(PbTe)_{1-2x}(PbSe)_x(PbS)_x$, eq 7 can be written as

$$w(x) = \frac{1}{\kappa(x)} = (1 - 2x)W_{PbTe} + x[W_{PbSe} + W_{PbS}] + (1 - 2x)x[C_{Te-Se} + C_{Te-S}] + x^2C_{Se-S} \quad (8)$$

where C_{Te-Se}, C_{Te-S}, and C_{Se-S} are the corresponding bowing factors for substituting Se and S to Te. Figure 11 shows the theoretical dependence of lattice thermal conductivity for the pseudo binary $(PbTe)_{1-x}(PbSe)_x$ system (top curve), and the pseudoternary $(PbTe)_{1-2x}(PbSe)_x(PbS)_x$ system (lower curve). As expected, additional alloying of PbTe with PbS will further reduce the lattice thermal conductivity. Interestingly, the experimental values for thermal conductivity for the pseudo ternary system are in good agreement with the theoretical curve, supporting the notion that the pseudo ternary $(PbTe)_{1-2x}(PbSe)_x(PbS)_x$ system does not have significant contributions from nanostructuring. The model and our experimental results indicate a maximum of 48% reduction (relative to that of pure PbTe) in κ_{latt} at room temperature.

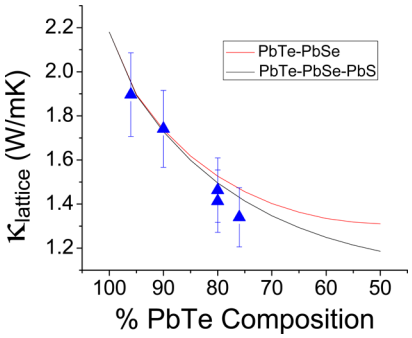

Figure 11. Comparison of the experimental lattice thermal conductivities and lattice thermal conductivities calculated based on point-defect, Umklapp, and normal scattering processes. The experimental data points (triangles) fall very close, within 10% error, to the theoretical lattice thermal conductivity curve for the pseudo ternary $(PbTe)_{1-2x}(PbSe)_x(PbS)_x$ pure solid solution. The calculated pseudo binary $(PbTe)_{1-x}(PbSe)_x$ lattice thermal conductivity (top curve) is similar to the calculated pseudo ternary lattice thermal conductivity (bottom curve) at high PbTe compositions.

Comparison to Other Systems. Figure 12 compares the thermal conductivity values for three lead chalcogenide alloy systems. The lowest value is observed in the $(PbTe)_{0.86}(PbSe)_{0.07}(PbS)_{0.07}$ system where κ_{tot} reaches 1.0 W/m·K . The $(PbTe)_{0.88(}PbS)_{0.12}$ reaches 1.1 W/m·K (ref 12) and $(PbTe)_{0.75}(PbSe)_{0.25}$ ≈1.2 W/m·K (ref 23). For the lattice contribution to thermal conductivity, PbTe−PbSe has the lowest reported value of 0.5 W/m·K but also has the highest electrical conductivity contributing to an overall highest total thermal conductivity for these alloyed materials.

In the $(PbTe)_{1-x}(PbSe)_x$ system, the high ZT of 1.8 is credited to the convergence of multiple degenerate valley pockets at the Fermi level.[22] Alloying PbTe with Se tunes the location of the valence band with temperature to effectively increase the density of states effective mass without negatively impacting the mobility leading to very high power factors and high ZT.[22] In contrast, the effects on the band structure are not clear when alloying PbTe with PbS. It is reasonable to expect that the substitution of S for Te atoms will lower the energy of the PbTe LHB and decrease the energy difference between the LHB and HHB thereby changing the transport properties. This lowering of the LHB enables the contribution of the recently discovered topological electrons[60] to give rise to the observed Seebeck plateau behavior.

Figure 13 compares the ternary $(PbTe)_{0.86}(PbSe)_{0.07}(PbS)_{0.07}$ material from this report with $(PbTe)_{0.75}(PbSe)_{0.25}$ from Pei et al.[22] and $(PbTe)_{0.88(}PbS)_{0.12}$ reported by Girard et al.[12] All three materials are doped with 2% Na and have comparable carrier concentrations between 0.5 and 1.6 × 10^{20} cm^{-3}. The conductivity and thermopower in Figure 13a,b show similar behavior for the $(PbTe)_{0.88(}PbS)_{0.12}$ and the $(PbTe)_{0.86}$-$(PbSe)_{0.07}(PbS)_{0.07}$ upon heating. The shape of the thermopower data curve upon cooling for $(PbTe)_{0.86}(PbSe)_{0.07}$-$(PbS)_{0.07}$, is similar to the $(PbTe)_{1-x}(PbSe)_x$ data, except the ternary system has higher values of 250 μV/K compared to 210 μV/K for the Se-alloyed binary. The steeper increase of the Seebeck coefficient at low temperatures may be explained by the different temperature dependence of the ΔE (energy gap between LHB and HHB) in the two samples. The similar valence band of the two PbS containing systems results in similar Seebeck behavior, but the higher conductivity for $(PbTe)_{0.86}(PbSe)_{0.07}(PbS)_{0.07}$ yields a power factor greater than either binary alloy system, as seen in Figure 13c.

In comparing the three systems in Figure 13, the Seebeck plateau clearly exists in the PbS containing systems but is absent in the PbTe−PbSe system. As mentioned above the

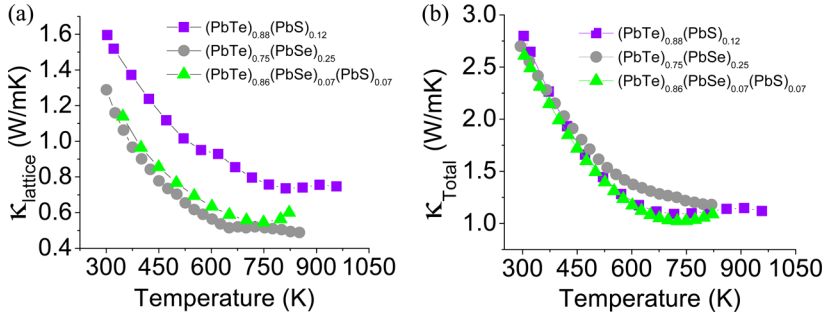

Figure 12. (a) Lattice thermal conductivity and (b) total thermal conductivity $(PbTe)_{0.75}(PbSe)_{0.25}$ (ref 23), $(PbTe)_{0.88}(PbS)_{0.12}$ (ref 7), and $(PbTe)_{0.86}(PbSe)_{0.07}(PbS)_{0.07}$ materials each doped with Na 2%. The reduction in κ_{total} is greatest for the pseudoternary system.

dx.doi.org/10.1021/ja4121583 | J. Am. Chem. Soc. 2014, 136, 3225−3237

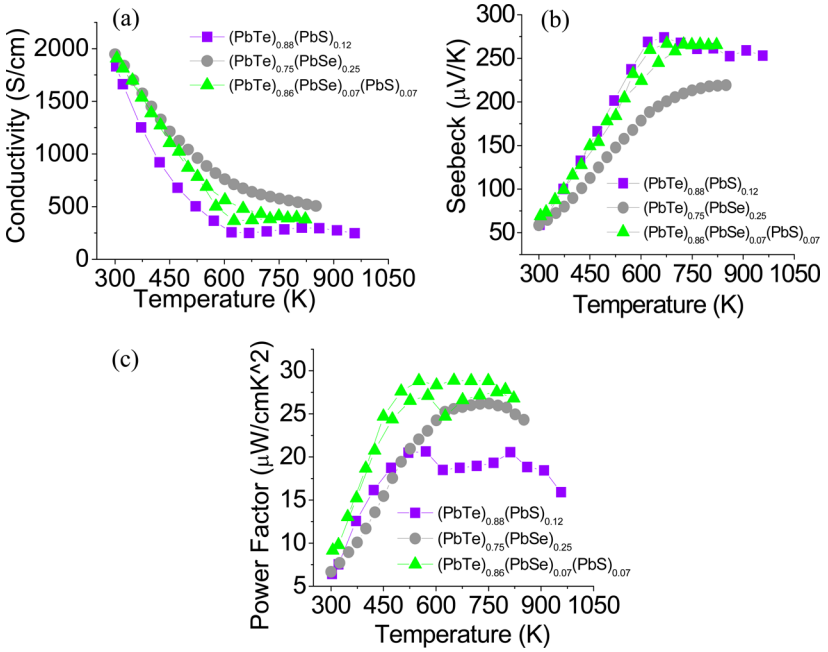

Figure 13. (a) Electrical conductivity, (b) Seebeck coefficient, and (c) power factor of $PbTe)_{0.75}(PbSe)_{0.25}$ (ref 23), $(PbTe)_{0.88}(PbS)_{0.12}$ (ref 12), and $(PbTe)_{0.86}(PbSe)_{0.07}(PbS)_{0.07}$ (both heating and cooling cycles) each doped with Na 2%. The plateau from 600 to 900 K in the Seebeck coefficient is present in the sulfur-containing systems but not $(PbTe)_{0.75}(PbSe)_{0.25}$. The pseudoternary alloy exhibits the highest power factor.

absence of a plateau in the PbTe−PbSe system likely arises because selenium does not lower the HHB of PbTe and its energy level remains inaccessible to the topological electrons. In the S analog, the LHB is lowered relative to the HHB, so the topological electrons are accessible in S-containing PbTe at a lower temperature than in pure or Se-containing PbTe, consistent with the experimental data. Therefore, sulfur is the more important component to observing this plateau behavior. Figure 14 shows *ZT* as a function of temperature for the three systems, and the 2% Na-doped $(PbTe)_{0.86}(PbSe)_{0.07}(PbS)_{0.07}$ material is the highest performing with *ZT* of 2.0 at 823 K.

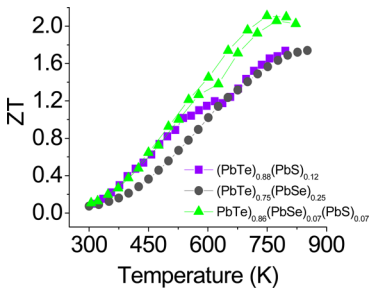

Figure 14. Figure of merit of $(PbTe)_{0.75}(PbSe)_{0.25}$ (ref 23), $(PbTe)_{0.88}(PbS)_{0.12}$ (ref 12), and $(PbTe)_{0.86}(PbSe)_{0.07}(PbS)_{0.07}$ doped with 2% Na. The heating and cooling cycle is shown for $(PbTe)_{0.86}(PbSe)_{0.07}(PbS)_{0.07}$, and the *ZT* upon cooling is slightly higher than the heating cycle.

CONCLUSIONS

The thermoelectric performance of the p-type pseudoternary $(PbTe)_{1-x-y}(PbSe)_x(PbS)_y$ system is superior to those of the corresponding the pseudobinary $(PbTe)_{1-x}(PbSe)_x$ and $(PbTe)_{1-x}(PbS)_x$ systems as well as those of the single phase p-type PbTe, PbSe, and PbS systems. Although the scope of any investigation of the $(PbTe)_{1-x-y}(PbSe)_x(PbS)_y$ system is very large due to the enormous composition space available, here we have presented an initial investigation and assessment of thermoelectric properties of selected p-doped samples with PbTe-rich compositions and equal molar fractions of PbSe and PbS. We have demonstrated that when the mole fractions of PbSe and PbS are <10% very high *ZT*s are possible, outperforming the simpler pseudobinary systems. Our study also uncovered that while very low lattice thermal conductivity can be achieved, e.g., for $(PbTe)_{0.86}(PbSe)_{0.07}(PbS)_{0.07}$, this reduction cannot be accounted for by nanostructuring but rather by highly effective point defect scattering involving a broad set of multiple types of point defects such as Te/S, Te/Se, and Se/S. These defects arise from the triple disorder created by the alloying of three different components in the rock-salt structure. The pseudoternary system's presumed higher entropy may favor a reduced nanostructuring, and this counterintuitive outcome is a sharp departure from the simpler pseudobinary systems of PbTe−PbS and PbSe−PbS where nanostructuring plays an important role. Undoubtedly, the $(PbTe)_{1-2x}(PbSe)_x(PbS)_x$ system is an excellent platform to study phase competition between entropically driven atomic mixing (solid solution behavior) and enthalpy driven phase separation. This completion is expected to be highly dependent on *x*. Nevertheless, given the small number of compositions investigated here additional work will be required to fully understand the nanoscale nature of this complex system.

ASSOCIATED CONTENT

Supporting Information

Description of multiple high-temperature thermoelectric measurements, diffusivity specific heat, and electronic thermal conductivity, and measured sample densities. This material is available free of charge via the Internet at http://pubs.acs.org.

dx.doi.org/10.1021/ja4121583 | J. Am. Chem. Soc. 2014, 136, 3225−3237

AUTHOR INFORMATION

Corresponding Author

m-kanatzidis@northwestern.edu

Notes

The authors declare no competing financial interest.

ACKNOWLEDGMENTS

We thank the Revolutionary Materials for Solid State Energy Conversion, an Energy Frontier Research Center funded by the U.S. Department of Energy, Office of Science, Office of Basic Energy Sciences, under Award No. DE-SC0001054, for primary funding. The TEM work made use of the EPIC facility (NUANCE Center, Northwestern University), which has received support from the MRSEC program (NSF DMR-1121262) at the Materials Research Center and the Nanoscale Science and Engineering Center (EEC-0118025/003), both programs of the National Science Foundation; the State of Illinois; and Northwestern University. Atom-probe tomography measurements were performed at the Northwestern University Center for Atom-Probe Tomography (NUCAPT), and the LEAP tomograph was purchased and upgraded with funding from the NSF-MRI (Grant No. DMR 0420532) and ONR-DURIP (Grant Nos. N00014-0400798, N00014-0610539, N00014-0910781) programs. NUCAPT is a shared facility of the Materials Research Center of Northwestern University, supported by the National Science Foundation's MRSEC program (Grant No. DMR-1121262).

REFERENCES

(1) Hsu, K. F.; Loo, S.; Guo, F.; Chen, W.; Dyck, J. S.; Uher, C.; Hogan, T.; Polychroniadis, E. K.; Kanatzidis, M. G. *Science* **2004**, *303*, 818.

(2) Perlt, S.; Hoche, T.; Dadda, J.; Muller, E.; Pereira, P. B.; Hermann, R.; Sarahan, M.; Pippel, E.; Brydson, R. *J. Solid State Chem.* **2012**, *193*, 58.

(3) Cook, B. A.; Kramer, M. J.; Harringa, J. L.; Han, M. K.; Chung, D. Y.; Kanatzidis, M. G. *Adv. Funct. Mater.* **2009**, *19*, 1254.

(4) Levin, E. M.; Cook, B. A.; Ahn, K.; Kanatzidis, M. G.; Schmidt-Rohr, K. *Phys. Rev. B* **2009**, 80.

(5) Poudeu, P. F. P.; D'Angelo, J.; Downey, A. D.; Short, J. L.; Hogan, T. P.; Kanatzidis, M. G. *Angew. Chem., Int. Ed.* **2006**, *45*, 3835.

(6) LaLonde, A. D.; Pei, Y.; Snyder, G. J. *Energy Environ. Sci.* **2011**, *4*, 2090.

(7) Pei, Y.; LaLonde, A.; Iwanaga, S.; Snyder, G. J. *Energy Environ. Sci.* **2011**, *4*, 2085.

(8) Wang, H.; Bahk, J. H.; Kang, C.; Hwang, J.; Kim, K.; Shakouri, A.; Kim, W. *J. Mater. Chem. A* **2013**, *1*, 11269.

(9) Zhang, Q.; Cao, F.; Liu, W. S.; Lukas, K.; Yu, B.; Chen, S.; Opeil, C.; Broido, D.; Chen, G.; Ren, Z. F. *J. Am. Chem. Soc.* **2012**, *134*, 10031.

(10) He, J.; Zhao, L.-D.; Zheng, J.-C.; Doak, J. W.; Wu, H.; Wang, H.-Q.; Lee, Y.; Wolverton, C.; Kanatzidis, M. G.; Dravid, V. P. *J. Am. Chem. Soc.* **2013**, *135*, 4624.

(11) Zhao, L.-D.; He, J.; Wu, C.-I.; Hogan, T. P.; Zhou, X.; Uher, C.; Dravid, V. P.; Kanatzidis, M. G. *J. Am. Chem. Soc.* **2012**, *134*, 7902.

(12) Girard, S. N.; He, J.; Zhou, X.; Shoemaker, D.; Jaworski, C. M.; Uher, C.; Dravid, V. P.; Heremans, J. P.; Kanatzidis, M. G. *J. Am. Chem. Soc.* **2011**, *113*, 16588.

(13) Girard, S. N.; He, J.; Li, C.; Moses, S.; Wang, G.; Uher, C.; Dravid, V. P.; Kanatzidis, M. G. *Nano Lett.* **2010**, *10*, 2825.

(14) He, J.; Blum, I. D.; Wang, H.-Q.; Girard, S. N.; Doak, J.; Zhao, L.-D.; Zheng, J.-C.; Casillas, G.; Wolverton, C.; Jose-Yacaman, M.; Seidman, D. N.; Kanatzidis, M. G.; Dravid, V. P. *Nano Lett.* **2012**, *12*, 5979.

(15) Biswas, K.; He, J.; Zhang, Q.; Wang, G.; Uher, C.; Dravid, V. P.; Kanatzidis, M. G. *Nat Chem* **2011**, *3*, 160.

(16) Biswas, K.; He, J.; Wang, G.; Lo, S.-H.; Uher, C.; Dravid, V. P.; Kanatzidis, M. G. *Energy Environ. Sci.* **2011**, *4*, 4675.

(17) Zhao, L.-D.; Hao, S.; Lo, S.-H.; Wu, C.-I.; Zhou, X.; Lee, Y.; Li, H.; Biswas, K.; Hogan, T. P.; Uher, C.; Wolverton, C.; Dravid, V. P.; Kanatzidis, M. G. *J. Am. Chem. Soc.* **2013**, *135*, 7364.

(18) Zhao, L.-D.; He, J.; Hao, S.; Wu, C.-I.; Hogan, T. P.; Wolverton, C.; Dravid, V. P.; Kanatzidis, M. G. *J. Am. Chem. Soc.* **2012**, *134*, 16327.

(19) Androulakis, J.; Todorov, I.; He, J.; Chung, D.-Y.; Dravid, V.; Kanatzidis, M. *J. Am. Chem. Soc.* **2011**, *133*, 10920.

(20) Johnsen, S.; He, J.; Androulakis, J.; Dravid, V. P.; Todorov, I.; Chung, D. Y.; Kanatzidis, M. G. *J. Am. Chem. Soc.* **2011**, *133*, 3460.

(21) He, J.; Sootsman, J. R.; Girard, S. N.; Zheng, J.-C.; Wen, J.; Zhu, Y.; Kanatzidis, M. G.; Dravid, V. P. *J. Am. Chem. Soc.* **2010**, *132*, 8669.

(22) Pei, Y.; Shi, X.; LaLonde, A.; Wang, H.; Chen, L.; Snyder, G. J. *Nature* **2011**, *473*, 66.

(23) Heremans, J. P.; Wiendlocha, B.; Chamoire, A. M. *Energy Environ. Sci.* **2012**, *5*, 5510.

(24) Pei, Y.; Wang, H.; Snyder, G. J. *Adv. Mater.* **2012**, *24*, 6125.

(25) Androulakis, J.; Todorov, I.; Chung, D.-Y.; Ballikaya, S.; Wang, G.; Uher, C.; Kanatzidis, M. *Phys. Rev. B* **2010**, *82*, 115209.

(26) Morelli, D. T.; Jovovic, V.; Heremans, J. P. *Phys. Rev. Lett.* **2008**, 101.

(27) Jaworski, C. M.; Wiendlocha, B.; Jovovic, V.; Heremans, J. P. *Energy Environ. Sci.* **2011**, *4*, 4155.

(28) Girard, S. N.; Schmidt-Rohr, K.; Chasapis, T. C.; Hatzikraniotis, E.; Njegic, B.; Levin, E. M.; Rawal, A.; Paraskevopoulos, K. M.; Kanatzidis, M. G. *Adv. Funct. Mater.* **2013**, *23*, 747.

(29) Kudman, I. *J. Mater. Sci.* **1972**, *7*, 1072.

(30) Seidman, D. N. *Rev. Sci. Instrum.* **2007**, 78.

(31) Seidman, D. N. *Annu. Rev. Mater. Res.* **2007**, *37*, 127.

(32) Seidman, D. N.; Stiller, K. *MRS Bull.* **2009**, *34*, 717.

(33) Miller, M. K.; Russell, K. F.; Thompson, K.; Alvis, R.; Larson, D. J. *Microsc. Microanal.* **2007**, *13*, 428.

(34) Pashinkin, A. S.; Mikhailova, M. S.; Malkova, A. S.; Fedorov, V. A. *Inorg. Mater.* **2009**, *45*, 1226.

(35) Blachnik, R.; Igel, R. *Z. Naturforsch., Teil B* **1974**, *29*, 625.

(36) McCarthy, T. J.; Kanatzidis, M. G. *Chem. Mater.* **1993**, *5*, 1061.

(37) Hohenberg, P.; Kohn, W. *Phys. Rev.* **1964**, *136*, B864.

(38) Kohn, W.; Sham, L. J. *Phys. Rev.* **1965**, *140*, A1133.

(39) Kresse, G.; Furthmüller, J. *Phys. Rev. B* **1996**, *54*, 11169.

(40) Blöchl, P. E. *Phys. Rev. B* **1994**, *50*, 17953.

(41) Perdew, J. P.; Burke, K.; Ernzerhof, M. *Phys. Rev. Lett.* **1996**, *77*, 3865.

(42) Monkhorst, H. J.; Pack, J. D. *Phys. Rev. B* **1976**, *13*, 5188.

(43) Doak, J. W.; Wolverton, C. *Phys. Rev. B* **2012**, *86*, 144202.

(44) Liu, H.; Chang, L. L. Y. *Mineral. Mag.* **1994**, *58*, 567.

(45) Alekseeva, G. T.; Prokof'eva, L. V.; Stil'bans, L. S. *Izv. Akad. Nauk SSSR, Neorg. Mater.* **1967**, *3*, 320.

(46) Gurieva, E. A.; Konstantinov, P. P.; Prokof'eva, L. V.; Ravich, Y. I.; Fedorov, M. I. *Semiconductors* **2003**, *37*, 276.

(47) Androulakis, J.; Pcionek, R.; Quarez, E.; Do, J.-H.; Kong, H.; Palchik, O.; Uher, C.; D'Angelo, J. J.; Short, J.; Hogan, T.; Kanatzidis, M. G. *Chem. Mater.* **2006**, *18*, 4719.

(48) (a) Quarez, E.; Hsu, K.-F.; Pcionek, R.; Frangis, N.; Polychroniadis, E. K.; Kanatzidis, M. G. *J. Am. Chem. Soc.* **2005**, *127*, 9177. (b) Bilc, D.; Mahanti, S. D.; Quarez, E.; Hsu, K. F.; Pcionek, R.; Kanatzidis, M. G. *Phys. Rev. Lett.* **2004**, *93*, 146403.

(49) Scanlon, W. W. *J. Phys. Chem. Solids* **1959**, *8*, 423.

(50) Veis, A. N.; Kaidanov, V. I.; Nemov, S. A. *Sov. Phys. Semicond.* **1980**, *14*, x.

(51) Volykhov, A. A.; Yashina, L. V.; Shtanov, V. I. *Inorg. Mater.* **2006**, *42*, 596.

(52) Tian, Z.; Garg, J.; Esfarjani, K.; Shiga, T.; Shiomi, J.; Chen, G. *Phys. Rev. B* **2012**, *85*, 184303.

(53) Ahmad, S.; Mahanti, S. D.; Hoang, K.; Kanatzidis, M. G. *Phys. Rev. B* **2006**, *74*, 155205.

(54) Airapetyants, S. V.; Vinograd, N. M.; Dubrovsk, I. N.; Kolomet, N. V.; Rudnik, I. M. *Soviet Phys. Solid State USSR* **1966**, *8*, 1069.
(55) Crocker, A. J. *J. Phys. Chem. Solids* **1967**, *28*, 1903.
(56) Ravich, U. I. *Semiconducting Lead Chalcogenides*; Plenum Press: New York, 1970.
(57) Smirnov, I. A.; Vinograd, M.; Kolomoet, N.; Sysoeva, L. M. *Sov. Phys. Solid State USSR* **1968**, *9*, 2074.
(58) Andreev, A. A.; Radionov, V. N. *Sov. Phys. Semiconductors* **1967**, *1*, 145.
(59) Jaworski, C. M.; Nielsen, M. D.; Wang, H.; Girard, S. N.; Cai, W.; Porter, W. D.; Kanatzidis, M. G.; Heremans, J. P. *Phys. Rev. B* **2013**, *87*, 045203.
(60) Singh, D. J. *Phys. Rev. B* **2010**, *81*, 195217.
(61) Ahmad, S.; Hoang, K.; Mahanti, S. D. *Phys. Rev. Lett.* **2006**, 96.
(62) Krakauer, B. W.; Seidman, D. N. *Phys. Rev. B* **1993**, *48*, 6724.
(63) Krakauer, B. W.; Seidman, D. N. *Acta Materialia* **1998**, *46*, 6145.
(64) Seidman, D. N. *Annu. Rev. Mater. Res.* **2002**, *32*, 235.
(65) Shashkov, D. A.; Seidman, D. N. *Phys. Rev. Lett.* **1995**, *75*, 268.
(66) Klemens, P. G. *Phys. Rev.* **1960**, *119*, 507.
(67) Wang, H.; LaLonde, A. D.; Pei, Y.; Snyder, G. J. *Adv. Funct. Mater.* **2013**, *23*, 1586.
(68) Abeles, B. *Phys. Rev.* **1963**, *131*, 1906.
(69) Zaitsev, V. K.; Tkalenko, E. N.; Nikitin, E. N. *Sov. Phys. Solid State USSR* **1969**, *11*, 221.
(70) Adachi, S. *J. Appl. Phys.* **1983**, *54*, 1844.
(71) Adachi, S. *J. Appl. Phys.* 2007, *102*.